Variability in the Gulf of Cadiz: Internal Waves and Globs

JAMES L. CAIRNS[1]

NATO Saclant ASW Research Centre, Viale San Bartolomeo 400, La Spezia, Italy

(Manuscript received 24 August 1979, in final form 3 January 1980)

ABSTRACT

An experiment was performed in the Gulf of Cadiz during June 1977, with the objective of separating oceanic variability due to internal waves from that due to inhomogeneities of the water. A CTD which oscillates in depth between 120 and 170 m while towed horizontally provides vertical (x,z) sections of temperature, salinity, density and sound velocity within this depth range. The density field is adequately resolved over long tow paths to give internal wave records in which the usual contamination due to horizontal and vertical thermal structure is minimized.

Identifying the effects of internal waves by their influence on the density field permits their removal from the records, leaving a clear picture of the variability within the medium due simply to spatial differences in the physical makeup of the water. The picture of the area investigated is one in which there are large cores of relatively cold fresh water scattered throughout a more uniform warmer, saltier background.

The size and expected persistence of such cores, together with the fact that their boundaries are marked by relatively strong gradients, add interest to their presence in the sound speed field. They account for only about one-fifth of the *overall* sound speed variance, but they may dominate it locally in the form of well-defined ducts tens of meters thick and several kilometers wide. On the whole, however, the major source of sound speed variability is the warping of the medium due to internal waves.

Although wave-induced fluctuations occur throughout the medium, their effects are not uniform. There is evidence of internal wave anisotropy in the Gulf, with propagation predominantly normal to the coast. In addition, with increased proximity to the coast the internal wave spectrum changes shape in a way that indicates a shift of energy to lower horizontal wavenumbers.

1. Introduction

Variability of the oceanic structure on vertical scales of meters to tens of meters, and horizontal scales of tens of meters to kilometers is thought to be dominated by two effects. First, the structure is characterized by interleaving globs of diverse water which sort themselves out slowly under the influences of gravity, friction and diffusion into a system of stable layers. They are evident as steplike irregularities typically found in oceanic vertical profiles of temperature and salinity. Second, additional variability arises from the continuous wobbling and straining of the whole layered system due to the action of internal waves. Although both waves and globs contribute to irregularities, their relative importance is not clear; their effects have been difficult to separate.

With improved techniques and understanding there have been some advances at making the separation, for example, the recent work of Joyce et al. (1978), Johnson et al. (1978) and Woods and Minnett (1979). As Johnson et al. point out, two types of globs are recognized: those which occur as

irregularities in the fields of temperature and salinity but not density, and those which cause irregularities in all three of these fields. We cannot distinguish between density wiggles due to internal waves and those due to other dynamical processes; therefore, an error is made in describing the wave field, and this error carries over into our description of the glob field.

The data discussed here consist of temperature, conductivity and depth profiles sampled in the (x,z) plane with adequate spacing along the x axis to describe the internal wave field. Wave effects are separated out and examined independently, in so far as possible, of irregularities in the background structure; the background is then examined without wave distortion.

2. Separation of effects

This section was developed in collaboration with Walter Munk. It is based on the technique of separating out motion effects by examining the variability of scalar properties along surfaces of consant potential density.

Let $S(z)$ and $\theta(z)$ designate the undisturbed distributions of salt and temperature (z positive downward). Our sensors move along a zig-zag path in the

TABLE 1. Values for a typical oceanic setting demonstrating the ratio of vertical displacement of temperature surfaces to potential temperature surfaces $(1 - \Gamma/\theta')$, and density surfaces to potential density surfaces $(1 - k/\rho')$.

Depth (m)	Tempera- ture (°C)	Salinity (‰)	Sound speed (m/s⁻¹)	Γ (°C m⁻¹)	k (cgs m⁻¹)	ρ' (cgs m⁻¹)	θ' (°C m⁻¹)	$(1 - \Gamma/\theta')$	$(1 - k/\rho')$
0	15.0	33.3	1500	1.6×10^{-4}	4.46×10^{-6}	7.32×10^{-6}	$-2. \times 10^{-2}$	1.01	0.39
1000	3.0	34.4	1480	0.80×10^{-4}	4.59×10^{-6}	4.98×10^{-6}	$-4. \times 10^{-3}$	1.02	0.08
2000	2.5	34.5	1490	0.89×10^{-4}	4.52×10^{-6}	4.57×10^{-6}	$-9. \times 10^{-4}$	1.10	0.01
3000	2.4	34.6	1510	1.06×10^{-4}	4.41×10^{-6}	4.41×10^{-6}	$-2. \times 10^{-4}$	1.53	0.00
4000	2.2	34.6	1525	1.22×10^{-4}	4.32×10^{-6}	4.32×10^{-6}	0	∞	0.00

x, z plane rapidly enough that the internal wave field can be thought of as fixed during the observations. We measure S and θ along the prescribed path $P(x,z)$, noting for salinity, for instance, the points $x(S)$, $z(S)$ along P where some particular salinity S is encountered. We shall use the shorthand $z_s(x)$ to denote the depth of the isohaline at horizontal distance x along the path.

It is useful to consider two hypothetical cases. In the first we assume internal wave motions of a field whose rest distributions of salt and temperature do not vary laterally. In the second we presume lateral variations of salt and temperature but no waves.

a. Case 1: waves only

For an upward[2] displacement $\zeta(x)$, the water parcel momentarily at z comes from a rest position $z + \zeta(x)$, and so

$$S(x,z) = \underline{S}[z + \zeta(x)]. \tag{1}$$

If we let z_0 designate the rest (mean) depth of water having a particular property, in this case, a particular salinity $S_0 \equiv \underline{S}(z_0)$, then we may write the inverse function as

$$z_{s_0}(x) = z_0 - \zeta(x), \tag{2}$$

where z_0 may be estimated by the average depth of $z_{s_0}(x)$ taken over the length of the measurement path. Thus, by measuring $z_{s_0}(x)$ we can generate $\zeta(x)$.

The same does not hold true for a nonconservative property of the water. For example,

$$\theta(x,z) = \underline{\theta}(z + \zeta(x)) - \Gamma\zeta(x), \tag{3}$$

where $\Gamma\zeta(x)$ is the temperature decrease of the raised water parcel due to adiabatic cooling. If $(d\theta/dz) < 0$, water of temperature θ is found somewhat shallower than the parcel which was raised by the wave a distance $\zeta(x)$ above z_0. Making the Taylor expansion [with $\theta_0 \equiv \underline{\theta}(z_0)$, $\theta' = d\theta/dz$] we may write approximately

$$\theta(x,z) = \theta_0 + [z_0 - \zeta(x) - z_{\theta_0}]\theta', \tag{4}$$

leading to the not particularly useful result

---

[2] The reader may object to the z axis being positive downward and the ζ axis positive upward but it proves to be the most convenient notation.

$$z_{\theta_0}(x) = z_0 - (1 - \Gamma/\theta')\zeta(x). \tag{5}$$

A more useful quantity is the *potential* temperature

$$\hat{\theta}(x,z) = \theta(x,z) + \Gamma\zeta(x). \tag{6}$$

Hence

$$\hat{\theta}(x,z) = \underline{\hat{\theta}}[z + \zeta(x)], \tag{7}$$

which is of the same form as (1), giving

$$z_{\hat{\theta}_0}(x) = z_0 - \zeta(x). \tag{8}$$

The amplitude of z_θ is $(l - \Gamma/\theta')$ times that of $z_{\hat{\theta}}$. Near the surface θ' is typically $-10^3\Gamma$, and so the isotherm is in phase with the displacement but of slightly greater amplitude (Table 1). At a depth where $\theta' \to \pm 0$ the isotherm amplitude approaches $\pm\infty$. At very great depth $\theta' \approx 0.9\Gamma$, and so the isotherm motion is very small and out of phase with the actual displacement. Of course, this is a result of the artificiality of θ as a tracer of the fluid.

Similarly for density we have

$$\rho(x,z) = \underline{\rho}[z + \zeta(x)] - k\zeta(x), \tag{9}$$

where $k\zeta(x)$ allows for the compressibility, leading to the result

$$z_{\rho_0} = z_0 - (1 - k/\rho')\zeta(x), \tag{10}$$

in which ρ' is generally positive.

Again we write

$$\hat{\rho}(x,z) = \rho(x,z) + k\zeta(x) \tag{11}$$

for the *potential* density, and so

$$z_{\hat{\rho}_0}(x) = z_0 - \zeta(x). \tag{12}$$

Near the sea surface ρ' is typically $2k$, and so z_ρ is in phase and half the amplitude of $z_{\hat{\rho}}$. At very great depth $\rho' \to 1.001k$, and z_ρ is in phase but small (Table 1).

The variation of S and $\hat{\theta}$ along surfaces of equal $\hat{\rho}$ in this case are zero: these are conservative quantities convected vertically with the internal wave motion.

We may wish (perhaps foolishly) to measure the salt and temperature variations along surfaces of equal ρ instead of $\hat{\rho}$. Substituting the expression (10) for z_{ρ_0} into (1) and (3), respectively, yields

$$S(x,z_{\rho_0}) = \underline{S}[z_{\rho_0} + \zeta(x)] = \underline{S}[z_0 + (k/\rho')\zeta(x)]$$

$$\approx S_0 + S'[k/\rho')\zeta(x)], \qquad (13)$$

$$\theta(x,z_{\rho_0}) \approx \theta_0 + \theta'(k/\rho')\zeta(x). \qquad (14)$$

Thus, even where the rest distributions of salt and temperature are independent of x one sees variations in θ and S along isopycnals. These are either in or out of phase with the wave motion depending on the signs of S' and θ'. For near-surface conditions $k/\rho' \approx \frac{1}{2}$, so the variations in S and θ along isopycnals are about half of the variations in $S(z_0,x)$ or $\theta(z_0,x)$ along some fixed depth z_0.

b. Case 2: globs, no waves

Again the sensor coordinates are known, and we observe the spatial variations in salt and potential temperature. The spatial distributions of S, θ are assumed frozen in time, implying $(dx/dt) \gg L/T$, where L and T are characteristic glob length and time scales.

Variability of salinity and potential temperature may be written as

$$\begin{aligned} \delta S(x,z) &= S(x,z) - \underline{S}(z) \\ \delta\theta(x,z) &= \theta(x,z) - \underline{\theta}(z) \end{aligned} \Bigg\} . \qquad (15)$$

These changes in salt and temperature may be associated with variations in potential density

$$\delta\hat{\rho}(x,z) = \hat{\rho}(x,z) - \underline{\rho}(z), \qquad (16)$$

where

$$\delta\hat{\rho} = \delta\hat{\rho}_s + \delta\hat{\rho}_\theta = b\delta S - a\delta\hat{\theta}, \qquad (17)$$

in which $a(\theta,S,p)$ and $b(\theta,S,p)$ are the coefficients of thermal expansion and haline contraction, respectively. The simplest case is that for which there is total compensation of salt and temperature, i.e.,

$$\begin{aligned} \delta\hat{\rho}(x,z) &= 0, \\ b\delta S(x,z) &= a\delta\hat{\theta}(x,z) \end{aligned} \Bigg\} . \qquad (18)$$

But there is no law of the sea that requires globs to be compensated. If they persist beyond an inertial period, we should expect the horizontal pressure gradients associated with a nonzero field of $\delta\hat{\rho}(x,z)$ to be largely balanced by geostrophic currents (or more precisely current shear). On the other hand, if the globs give rise to density inversions, we should expect these to be eliminated rather quickly—in a time of the order of the buoyancy period. Thus in regions of intensive temperature and salinity inversions we expect at least a partial compensation to the extent required to eliminate density instabilities.

c. Combined effects: waves and globs

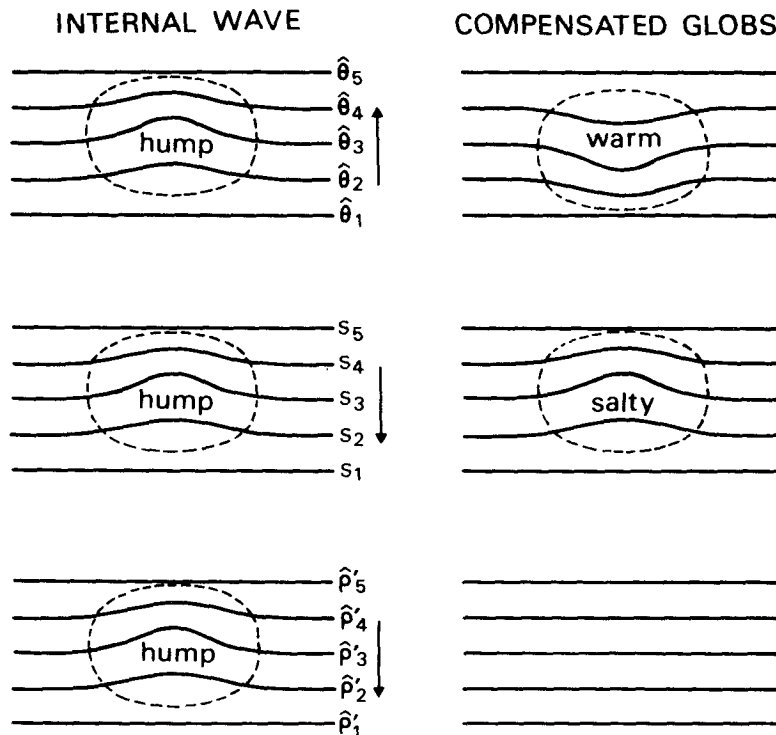We can separate the combined effects for the case of complete compensation (Fig. 1). Then the vertical

FIG. 1. Contours of potential temperature, salinity and potential density in a vertical section (x,z) for an internal wave hump and a compensated warm, salty glob, both localized in x and z. The potential temperature increases upward; the salinity and potential density increase downward.

displacements of constant $\hat\rho$ surfaces are due entirely to the up and down motion of internal waves, i.e.,

$$z_{\hat\rho_0}(x) = z_0 - \zeta(x), \qquad (19)$$

whereas the fluctuations of salinity and potential temperature along these surfaces are due entirely to globs,

$$\left. \begin{array}{l} S(x,z_{\hat\rho_0}) = S_0 + \delta S(x,z_0) \\ \hat\theta(x,z_{\hat\rho_0}) = \hat\theta_0 + \delta\hat\theta(x,z_0) \end{array} \right\} . \qquad (20)$$

Here $\delta S(x,z_0)$, $\delta\hat\theta(x,z_0)$ represent the glob field one would observe in the absence of waves.

It is helpful to derive this result systematically. The combined field may be written

$$\left. \begin{array}{l} S(x,z) = \underline{S}[z + \zeta(x)] + \delta S[x, z + \zeta(x)] \\ \hat\theta(x,z) = \underline{\hat\theta}[z + \zeta(x)] + \delta\hat\theta[x, z + \zeta(x)] \end{array} \right\} . \qquad (21)$$

Multiplying the first equation by b and the second by a and adding leads to

$$\hat\rho(x,z) = \underline{\hat\rho}[z + \zeta(x)] + \delta\hat\rho[x, z + \zeta(x)]. \qquad (22)$$

For complete compensation $\delta\hat\rho = 0$, giving

$$\hat\rho(x,z) = \underline{\hat\rho}[z + \zeta(x)] \qquad (23)$$

$$z_{\hat\rho_0}(x) = z_0 - \zeta(x). \qquad (24)$$

Substituting $z_{\hat\rho_0}$ for z in (21), and allowing for the fact that we can replace $z_{\hat\rho_0} + \zeta(x)$ by z_0 in each of the four arguments on the right-hand side leads to the result (20).

This separation depends on the fact that $z_{\hat\rho}$ (but not z_θ or z_s) follows the wave motion. But if compensation of salt and temperature effects is not complete then $z_{\hat\rho}$ no longer does. If we assume complete compensation and it does not exist, we wrongly assign some of the $z_{\hat\rho}$ fluctuations to internal waves, whereas they may represent inclinations of the density field balanced by other dynamical processes (i.e., geostrophic current shear). This also causes some errors in our portrayal of the glob field. The separation depends on the fact that, in the absence of waves, surfaces of constant density $z_{\hat\rho}$ are flat. We look along these $z_{\hat\rho}$ surfaces at the variability and say that it is the variability that one would see along the flat surface if there were no waves. But if the $z_{\hat\rho}$ surface is not flat in the absence of waves, we are really seeing the variability along an inclined surface. If this residual warping of the $z_{\hat\rho}$ surface is small, our resulting picture of the glob field will not be distorted much. This is thought to be the case. We believe the general situation is that

$$\left\{ \begin{array}{l} z_{\hat\rho} \text{ fluctuations due to} \\ \text{other processes} \end{array} \right\} \ll \left\{ \begin{array}{l} z_{\hat\rho} \text{ fluctuations due to} \\ \text{internal waves} \end{array} \right\},$$

and that concerning the physical properties of the medium

$$\left\{ \begin{array}{l} \text{variability due to} \\ \text{uncompensated globs} \end{array} \right\} \ll \left\{ \begin{array}{l} \text{variability due to} \\ \text{compensated globs} \end{array} \right\}$$

$$< \left\{ \begin{array}{l} \text{variability due to} \\ \text{internal waves} \end{array} \right\} .$$

3. The experiment

The measurements were made with a towed, vertically oscillating instrumentation package (TOB) having sensors and electronics from a Plessey model 9400 CTD. It was designed for towing at modest speeds (<5 kt) to depths no greater than 400 m. A more complete description of the TOB is in preparation by F. De Strobel. It is sketched along with its towing arrangement in Fig. 2.

There are two essential features of the TOB design. One is that it is constrained to move up and down on a cable held taut by a heavy depressor weight which gives stability to the system. The weight can be as heavy as desired; it does not have to be hauled up and down with every TOB profile. The oscillations of the TOB itself can then be accomplished with a small lightweight winch. The other essential feature is that the TOB sensor frame pivots around a rotational point near its center. Vanes on the rear of the frame stabilize it and cause it to rotate so that the sensors point directly into the flow. The sensors are always out in front of the guide cable (and everything else), and receiving the flow straight on.

While towed at 2 kt, the instrument package oscillated in depth along the guide cable between 120 and 170 m. Average vertical sensor speed was 1 m s^{-1}; instantaneous speed varied somewhat due to ship pitching. The sensor path in space was nominally a 45° zig-zag line. Only the upward traveling TOB profiles were used in the analysis, giving on average a profile of 50 m vertical extent every 100 m along the ship track.

The routes along which the tows were made were determined by satellite navigation; they are shown in Fig. 3. Data segments in the figure are numbered in the sequence in which they were measured. The weather and sea were calm during tow segments 2 and 3. By the middle of segment 4, a 30 kt wind blew from the northwest, becoming lighter near the end of segment 7. Strong offshore winds (25 kt) were encountered along 8. Water depth ranged from 500 m along the most shallow part of the route (segment 8) to 2500 m at the end of segment 5. Total length of the tow segments along which data were taken is ~350 km, a distance covered in 106 h beginning on 26 June 1977.

Temperature, conductivity and pressure were simultaneously sampled eight times per second (every 12 cm vertically) and recorded as 16-bit binary coded numbers on magnetic tape. Their least count
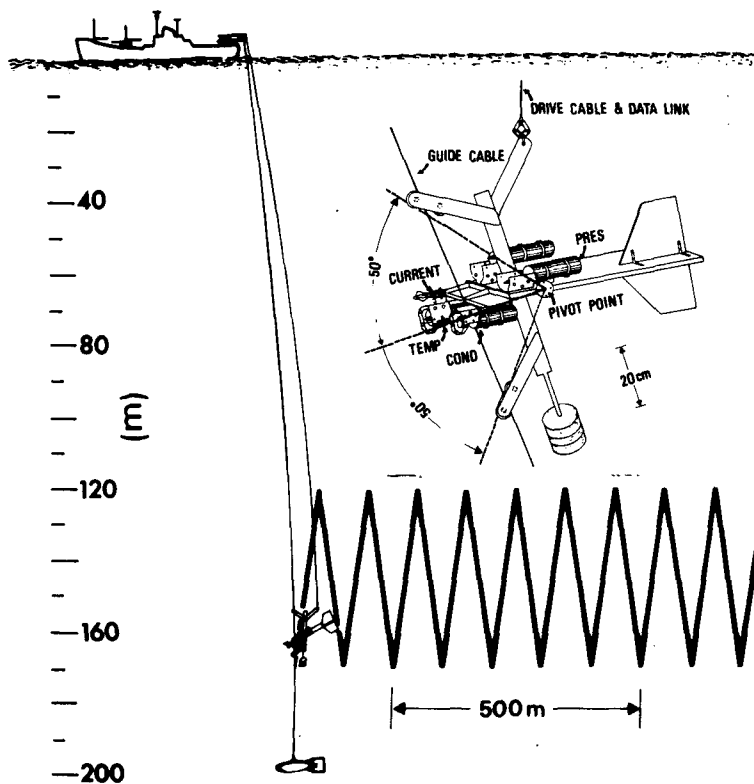
FIG. 2. A sketch of the TOB and its towing arrangement.

precisions are ±0.002°C, ±0.002 mS cm⁻¹, and ±0.034 m (equivalent water depth), respectively. Time constants for the temperature, conductivity and pressure probes are 0.4, 0.1 and 0.1 s. The data were filtered to minimize the effects of the pitching ship, and the temperature series was time shifted relative to the others by 3.7 s to best account for the different sensor time constants. The filtering resulted in a vertical wavenumber cutoff of 0.07 cpm (cycles per meter). Salinity, density and sound speed were then computed from the adjusted data.

Density and sound speed profiles of the upper kilometer (Fig. 4) give an idea of the gross structure in the area. They are from a CTD cast taken at the end of tow segment 5.

A variety of oceanic structures was encountered along the tows. Fig. 5 shows a section of profiles demonstrating a quiet region along track 8. Each profile on the figure is a graph of one of the variables versus depth. The scale for each variable is positioned to refer to the first profile; successive profiles have then been plotted by shifting the scale to the right a fixed distance (equal to 100 m along the x path). On each profile the depths of encounter of particular values of the variables were registered, so that lines passing from profile to profile through these depths give the changing elevation of the isopleths along the tow.

In contrast to the relatively quiet section shown in Fig. 5, Fig. 6 depicts one of the most active regions. It is from tow segment 4. The fields of temperature, salinity and sound speed appear folded into complex patterns with inversions tens of meters thick and several kilometers in horizontal extent. The potential density field on the other hand, which pre-
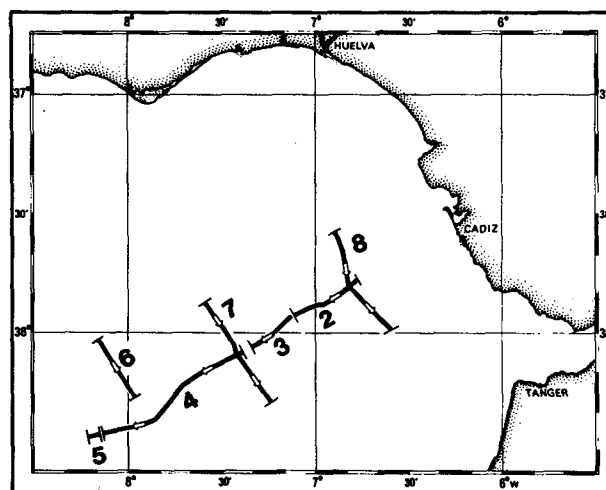

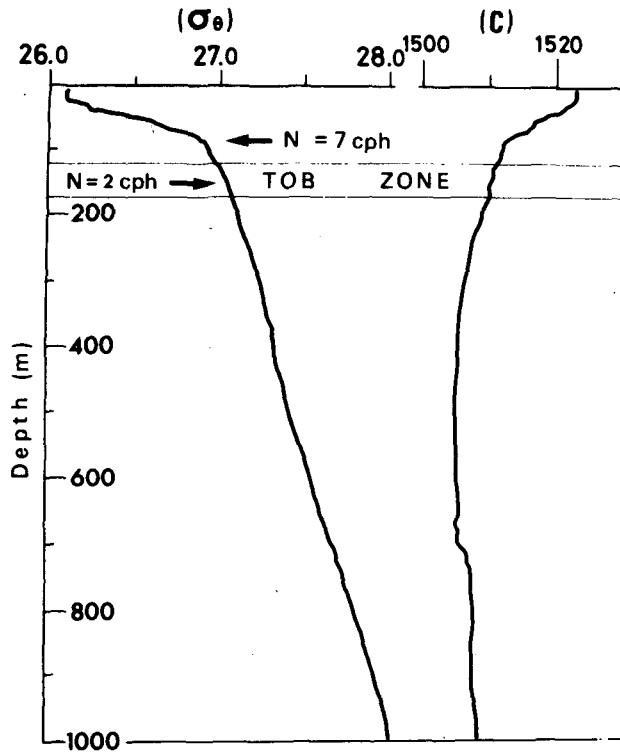FIG. 3. Area map of the experiment showing TOB tow segments 2–8 in the order taken.

FIG. 4. Profiles of sound speed (m s^{-1}) and potential density (g cm^{-3}) in the upper 1000 m taken from a CTD cast at the end of tow segment 5. $\sigma_\theta = (\rho_\theta - 1.0)1000$.

sumably is distorted only by wave activity, shows no evidence of these folds.

As will be seen in later figures, complex structures such as these were found scattered throughout the area. In such regions, there is little correspondence between the isothermal or isohaline surfaces and surfaces of constant potential density.

4. Internal wave spectra

One of the primary motivations for this work was to obtain internal wave wavenumber spectra with a minimum of contamination by vertical or horizontal finestructure. Profiling vertically removes the need for interpolation between sensors, or for assuming properties of vertical gradients—two problems typically associated with towed measurements. In addition, estimating the wave records from potential density surfaces rather than potential temperature surfaces decreases contamination due to range-dependent features of the sea's structure. We are still faced with the fact that not all wrinkles in the potential density surfaces are wave related, but this is thought to be a smaller source of contamination which occurs in addition to those just mentioned.

Wave records are computed from the measured data as follows. For each tow segment 2–8 shown in Fig. 3, we calculate the overall average potential density encountered at our mid-range depth of 145 m.

Having established that density value, each profile of a tow segment is then searched to determine the local depth of that density, resulting in series $z_\beta(x)$. The series are not sampled equally along x, so we resample them at a fixed sample interval (100 m) using linear interpolation. The corresponding $\zeta(x)$ series are then obtained using (12).

The wavenumber spectrum of $\zeta(x)$ based on all of the data segments is shown in Fig. 7. Estimates from the Garrett Munk model are consistent with the overall spectrum to within factors of 2 or so (Garrett and Munk, 1972, 1975; Cairns and Williams, 1976; Desaubies, 1976).

a. Directionality

There are differences in the internal wave energy level from various segments of the tow. Fig. 8
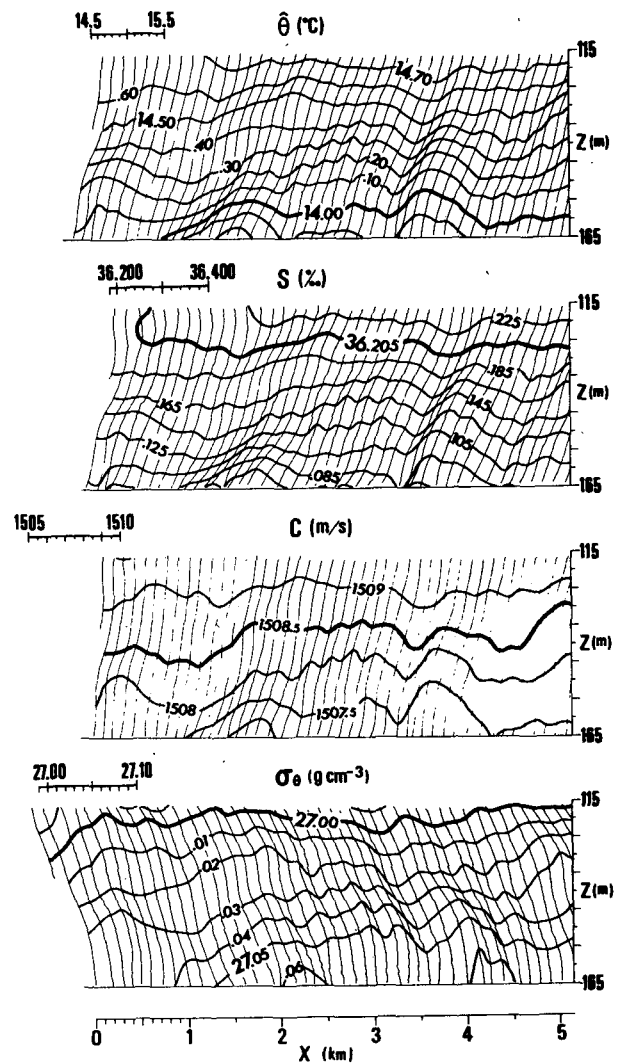

FIG. 5. Sequential profiles of potential temperature, salinity, sound speed and potential density showing isopleths along 5 km of tow segment 8.
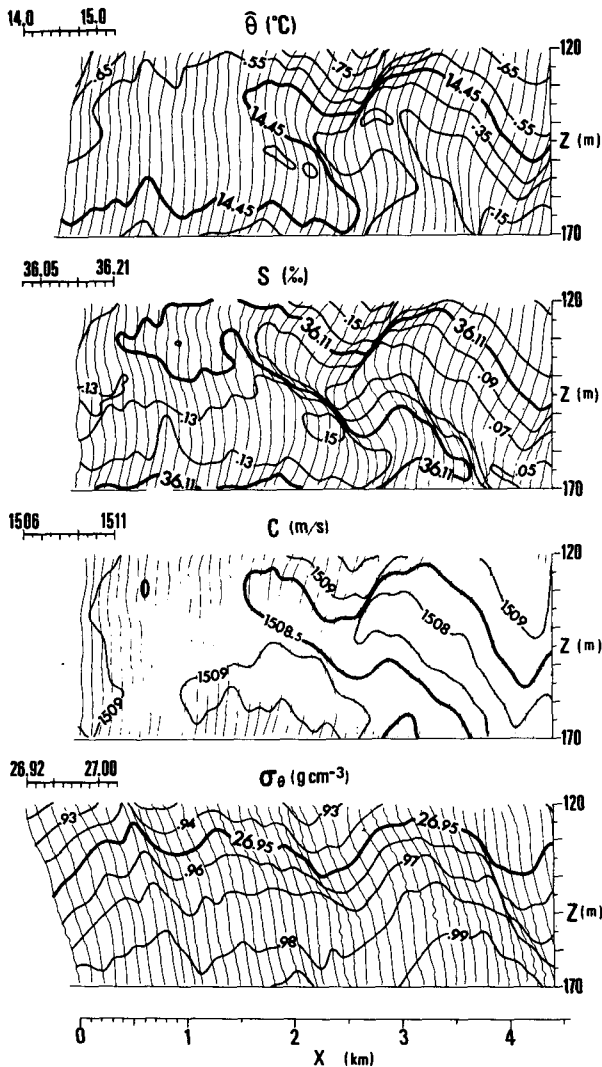
FIG. 6. Sequential profiles as in Fig. 5 shown here for a part of tow segment 4.
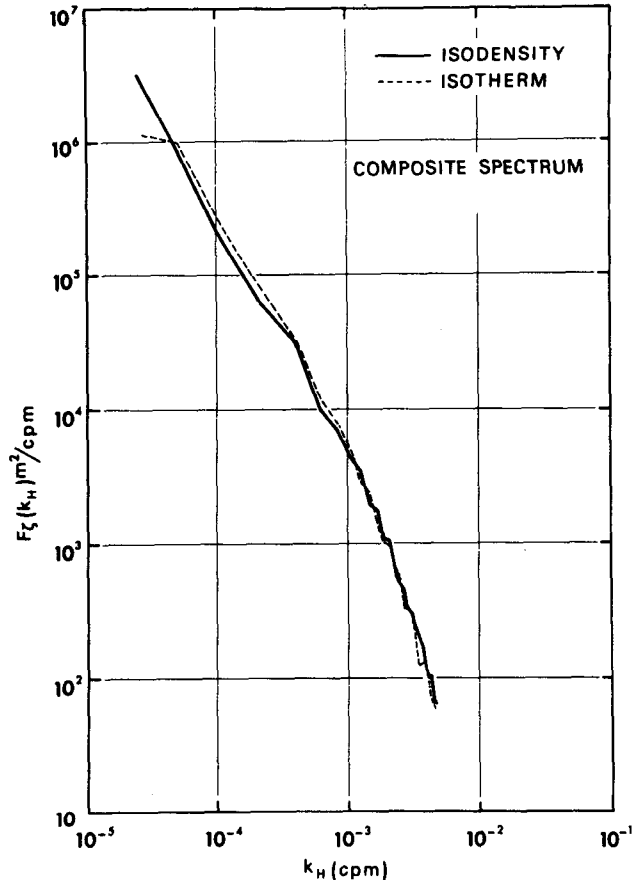

FIG. 7. Horizontal wavenumber spectrum of internal wave displacement based on all data segments. Solid curve is based on potential density surface. Dashed curve is based on potential temperature surface. Degrees of freedom range from 6 to 104.

b. Spectral shape

Wavenumber spectra estimated from various parts of the long offshore tow track (segments 2, 3, 4, 5) show that the spectral shape changes with

gives the mean displacements (ζ_{rms}), showing a disparity between wave displacement on the tows taken roughly parallel to the bottom contours (segments 6, 7, 8), and those made perpendicular to these contours (segments 2, 3, 4, 5). Overall, ζ_{rms} for the offshore tows is 7.0 m, whereas for the alongshore tows it is 5.6 m. This dependence of energy level on tow direction indicates anisotropy of the wave field, with more wave energy directed onshore-offshore than parallel to shore.

Additional evidence for internal wave directionality in the Gulf of Cadiz has been presented by Stevenson (1977). Visual photographs from Skylab 2 (July 1973) and from the Apollo spacecraft (July 1975) both show surface slicks interpreted as wave effects. These are oriented more or less along the bathymetric contours, indicating propagation normal to shore.
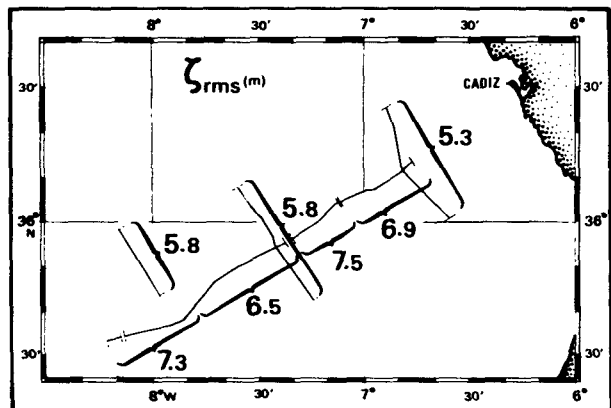

FIG. 8. rms internal wave displacement along various parts of the ship track.
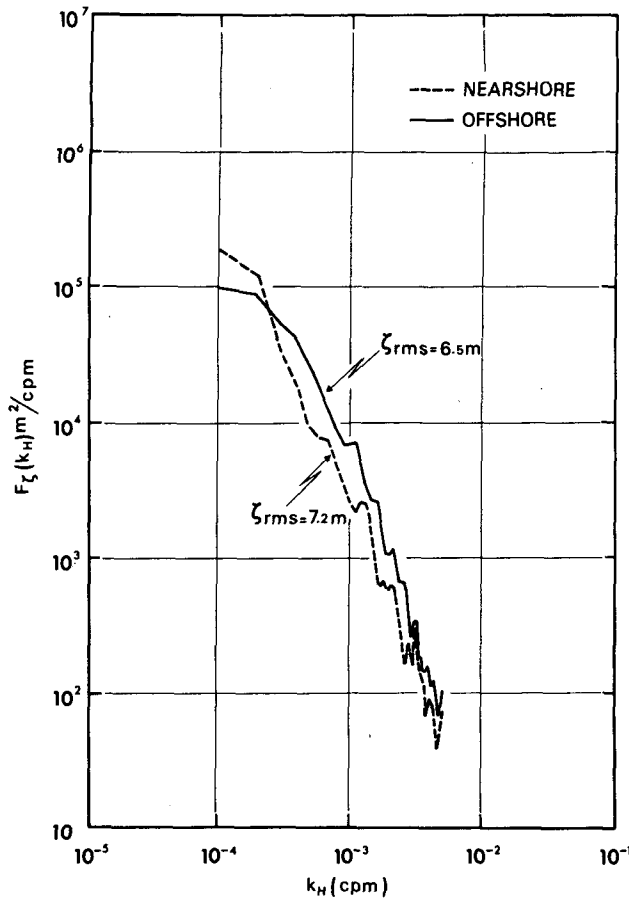
FIG. 9. Horizontal wavenumber spectra from the nearshore (segments 2 and part of 3 as seen in Fig. 3), and the offshore (part of segment 3, and segments 4 and 5) portions of the long tow directly away from the coast. Spectra have 25 and 50 degrees of freedom, respectively.

distance from shore (and with water depth). Plots of $\zeta(x,z)$, which will be discussed in a later section (Fig. 12), indicate that there is more low-wavenumber energy and less high-wavenumber energy in the internal wave field in the shallower nearshore region than there is farther away from shore. The transition appears to occur midway along segment 3 (of Fig. 3). Fig. 9, which illustrates spectra based on the wave records from either side of the transition, shows this change in spectral shape. The integrated energies of the two spectra differ only slightly.

c. Contamination

Most existing internal wave observations have been made using temperature rather than density as a tracer of the motion. To examine the validity of this method we have constructed series $z_\theta(x)$ from the measurements. When forming the series, where a particular isotherm was encountered more than once on a single profile, as in Fig. 6 for example,

its mean depth on the profile was used. Although profiling rather than towing sensors at fixed depth minimizes contamination of $z_\theta(x)$ due to vertical finestructure, the resulting series are still distorted by horizontal temperature structure. Comparison in Fig. 7 of the power spectrum estimated from $z_\rho(x)$, which is not affected by horizontal structure, with that of $z_\theta(x)$, which is affected, suggests that the power spectrum estimate is not too sensitive to the contamination. In that case, for estimates of horizontal wavenumber spectra, one does about as well to use potential temperature as potential density to describe the wave motion.

5. Glob and wave records

In this section we discuss figures which portray the fields of salt and temperature anomalies due to globs (Figs. 11 and 13), and others which describe the separate anomaly fields due to internal waves (Figs. 12 and 14). Interpretation of these requires some explanation of their construction.

Eqs. (19) and (20) when used for values of z_0 chosen at 2.5 m intervals between 120 and 170 m determine the (x,z) fields of ζ, $\delta\hat{\theta}$ and δS. Since the mean values $\hat{\theta}_0$ and S_0 are removed at each depth z_0, $\delta\hat{\theta}(x,z)$ and $\delta S(x,z)$ represent irregularities about the mean profiles $\hat{\theta}(z)$, $\underline{S}(z)$ where these are averages over some length of path. For convenience paths 10 km long are analyzed here whenever possible, but since the mean profiles change only slowly from place to place the results are rather insensitive to path length.

Fig. 10 shows data including the same tow segment previously seen in Fig. 6. The reference rest depths z_0 are indicated on the two upper graphs in Fig. 10 by horizontal dashed lines wherever the potential density surface z_ρ with rest depth z_0 is within the TOB's field of view (i.e., 120 m $< z_\rho < 170$ m). When a density surface is out of the TOB's range, no information is available for it, and the corresponding dashed line along its rest depth is omitted. Along the remaining dashed line regions we have measurements of ζ, $\delta\hat{\theta}$ and δS. We may represent δS and $\delta\hat{\theta}$ on a single graph, since along an isopotential density surface

$$\delta S = ab^{-1}\delta\hat{\theta}. \tag{25}$$

Using local values of a (0.2 × 10^{-3} °C^{-1}) and b (0.8 × 10^{-3} ‰$^{-1}$) gives $\delta S = 0.25 \, \delta\hat{\theta}$.

Defined in this manner, $\delta\hat{\theta}$ and δS are the range-dependent anomalies in the undisturbed fields of potential temperature and salt, and $\zeta(x,z)$ is the internal wave displacement field. We may compare wave-caused disturbances in the temperature field, for instance, with the irregularities $\delta\hat{\theta}$ existing in the undisturbed field. We approximate the wave effects as

$$\delta\hat{\theta}_w(x,z) = (d\hat{\theta}/dz)\zeta(x), \qquad (26)$$

where $d\hat{\theta}/dz$ ($\approx 0.01°\text{C m}^{-1}$) is the undisturbed potential temperature gradient.

The potential temperature at any point is then approximately written as

$$\hat{\theta}(x,z) = \hat{\theta}(z) + \delta\hat{\theta}(x,z) + \delta\hat{\theta}_w(x,z). \qquad (27)$$

It is instructive to compare the different ways of displaying the same data. The up and down motions of the density surfaces in the lower panel of Fig. 10 are easily related to the wave displacement contours in the upper panel. Changes in the temperature field $\hat{\theta}(x,z)$ in Fig. 10 can be associated with the combined glob and wave effects shown in the upper panels, which sum to give the variations in temperature about the mean temperature profile. To reiterate, then, the upper panel in Fig. 10 shows wave displacement $\zeta(x,z)$. The graph of Fig. 10 labeled "glob effect" is variability about the mean profile due to differences in the makeup of the water in its rest condition. Multiplying $\zeta(x,z)$ by the vertical gradient of a conservative scalar $(\hat{\theta},S,\hat{C})$ gives the wave-induced variability in the field of that property.

Figs. 11 and 13, then illustrate variations of salt and potential temperature about the mean conditions of the undisturbed field. In Fig. 11 is shown $\delta\hat{\theta}$ (or $\delta\hat{S}$) for all the offshore tow segments (2, 3, 4 and 5 of Fig. 3). These segments are further divided into pieces 10 km or so long, and are shown in the order reading left to right, top to bottom that they were taken as the tow proceeded offshore. The pieces are loosely joined to each other, because some data are lost between them in the processing.

a. Glob records

In the nearshore regions (numbers 2 and 3 in Fig. 11) there is little glob activity so that only one or two contour intervals above or below zero occur, although a warm salty core of water is seen in the last panel of segment 3. Section 4Ib shows a relatively weak cold fresh core, and in the remainder of segment 4 and throughout segment 5 there are pronounced cores of relatively cold fresh water. Except for the warm salty patch in segment 3, the structure seems to consist of cores of cold fresh water embedded in a more uniform relatively warm, salty background.

Fig. 13 gives the corresponding record for the perpendicular tow paths (6, 7 and 8 of Fig. 3). These show the same sorts of patterns as Fig. 11: low glob variability near the coast in path 8, and cold fresh cores of water in paths 6 and 7.

Temporal scales may be estimated for these globs based upon their sizes, provided that their destruction results from diffusion. According to Johnson
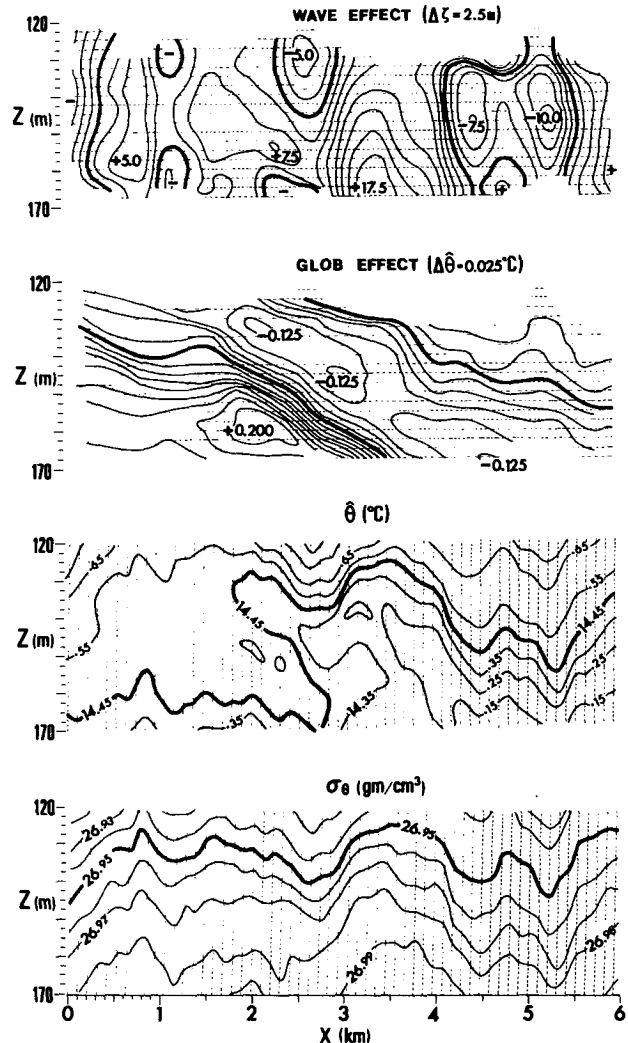

Fig. 10. Density and potential temperature fields from part of tow segment 4. The upper panel shows the field of $\zeta(x,z)$. The panel $\delta\hat{\theta}(x,z)$ below it shows the thermal variability due to inhomogeneities after the wave effects have been removed. Contour interval $\Delta\zeta = 2.5$ m; $\Delta\hat{\theta} = 0.025°\text{C}$.

et al. (1978), such a feature of thickness l will dissipate to $1/e$ of its strength in time $t = l^2/4\pi^2 K_z$, where K_z is the coefficient of diffusion. They estimate K_z values ranging from 1.4×10^{-7} m^2 s^{-1} (molecular) to 3.7×10^{-5} m^2 s^{-1} [turbulent, based on Gregg et al. (1973)]. Lifetime estimates for the cores shown here, if we take them typically to be 30 m thick, thus range from one week to five years!

The limited vertical extent of our measurements, when compared to the vertical wavenumber cutoff of the processed data, offers little opportunity for a statistical description of the globs. In spite of this, the crudest estimate of their mean height to length ratio $\langle r \rangle$ is put forward here because it is a quantity of some interest (Dashen, 1977), and because few

estimates of the ratio are known. The estimate is made by taking the mean ratio of vertical to horizontal extent of all of the closed contours in Figs. 11 and 13. We find very nearly that $\langle r \rangle = 1/50$, with values of r ranging between the extremes of 1/10 to 1/170.

b. Wave records

Variability due to waves is shown in Figs. 12 and 14. Wave activity occurs throughout the records, and not in patches as did the globs, and for a given vertical size, wave-caused irregularities are seen to
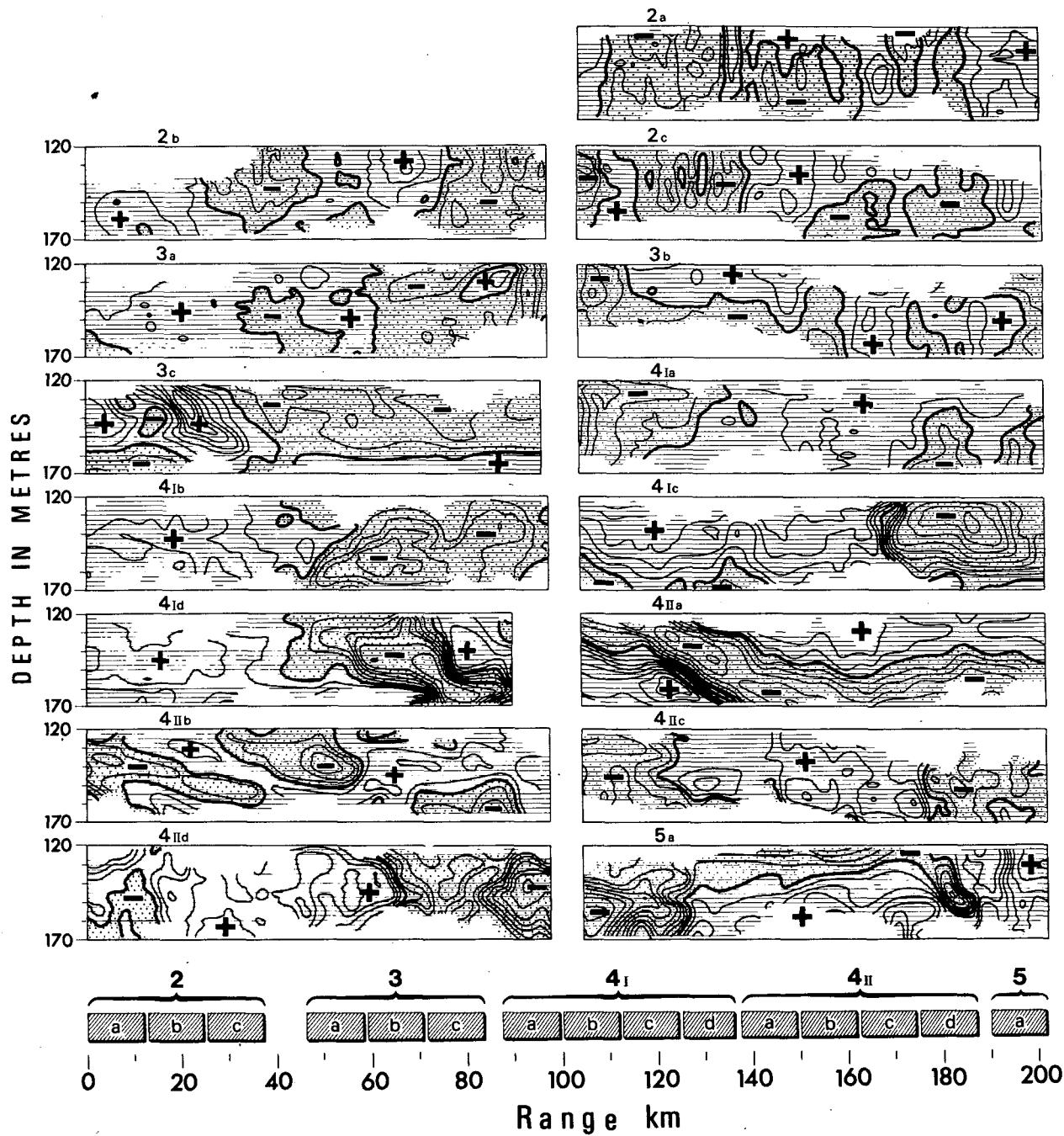

FIG. 11. Variations of the sea's properties due to inhomogeneities. Observations are along segments of the offshore tow path. The lower bar graph shows the locations of the observations along the tow path. The contours may be interpreted in terms of potential temperature ($\Delta \theta = 0.025°C$), or salinity ($\Delta S = 6.3 \times 10^{-4}$ ‰), or potential sound speed ($\Delta \hat{C} = 0.1$ m s^{-1}). Viewing window excludes vertical wavelengths < 14 m and horizontal wavelengths < 250 m.

have relatively smaller horizontal scales than those of globs. The extremes of anomalies due to the two causes, however, are about equal. Wave-induced fluctuations have different time scales than globs, ranging from ~1 h (the buoyancy period) to ~1 day (the local inertial period).

In Fig. 12 a difference in the internal wave field is noted between the nearshore and offshore regions. Nearshore records. (panels 2a, b, c and 3a, b) indicate relatively little wave activity at high horizontal wavenumbers, the energy appearing to be concentrated in longer waves. Further offshore
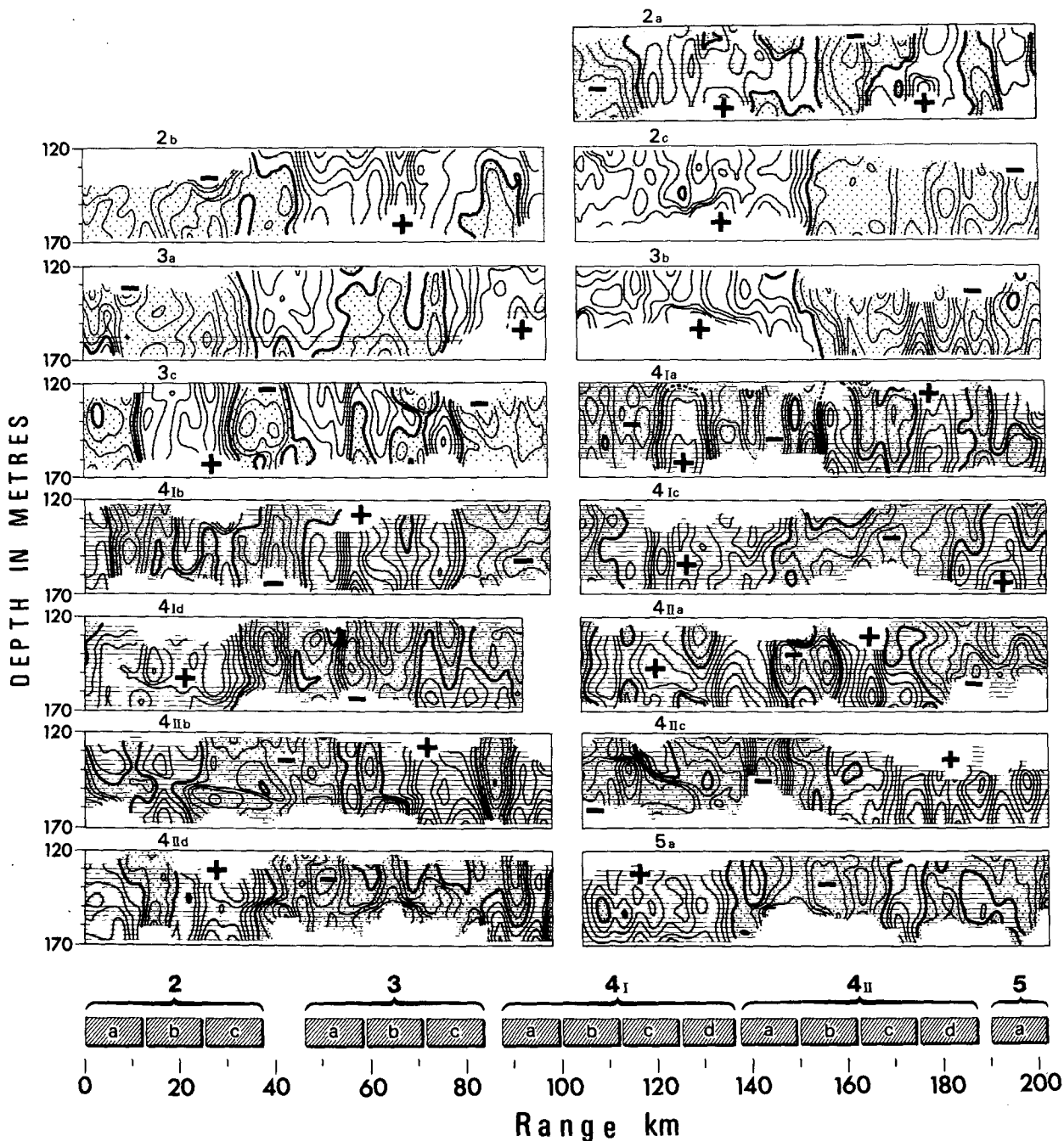

FIG. 12. The internal wave displacement field $\zeta(x,z)$. Observations are along segments of the offshore tow path. The lower bar graph shows the locations of the observations along the path. The contour interval $\Delta \zeta = 2.5$ m. These contours may also be interpreted in terms of the wave induced variability in the fields of salt ($\Delta S = -5.5 \times 10^{-3}$ ‰), potential temperature ($\Delta \hat{\theta} = -0.035°C$) or potential sound speed ($\Delta \hat{C} = -0.1$ m s^{-1}) by using relations like Eq. (26). Viewing window excludes vertical wavelengths < 14 m and horizontal wavelengths < 250 m.

(panels 3c; 4Ia,b,c,d; 4IIa,b,c,d; and 5a) there is relatively greater wave activity at high wavenumbers. Fig. 9 gives a more concise description of this difference. There is no obvious causal relationship between this change in the wave field and features of weather or bottom topography. The sea deepens more or less uniformly over the length of the offshore tow, and the observed weather change occurred later than the change in the wave field.

Our observations of the wave and glob fields in the Gulf are briefly summarized as follows. The background variability consists mainly of cores of cold fresh water imbedded in a more uniform warm salty background. These are typically tens of meters thick and several kilometers long. They have lifetimes of weeks or more.

Superimposed on this background is the variability due to internal waves. The extreme magnitudes of the two types of irregularities are about the same size, but internal wave effects occur throughout the area, not just here and there as do glob effects, and patterns of variability due to waves may change from hour to hour.

6. Double diffusive effects

We may interpret the structure observed in Figs. 11 and 13 as cold fresh intrusions leaking into a warmer saltier background. In such a setting, double diffusive processes are expected to play an important role in determining the anatomy of the intrusions. Some features of the observed structure are indeed suggestive of these processes.

Cold fresh intrusions have lower boundaries sharpened by the diffusive regime, and upper boundaries destabilized by the salt-fingering regime of the doubly diffusive system. [Warm salty intrusions undergo the same effects in the opposite sense (Turner, 1978).] Some evidence of this inequality of gradients has been seen in the oceanic measurements of Howe and Tait (1972), Gregg and Cox (1972) and Gargett (1976).

An additional effect may result from the unequal exchange of buoyancy across the upper and lower boundaries, a greater buoyancy flux occurring across the more active fingering interface. As Turner points out, cold fresh intrusions in this case would likely become heavier with age developing a downward tilt across isopycnals. Howe and Tait (1970) found hot salty intrusions to rise across isopycnals away from their source with a slope of order 10^{-2}.

The cold fresh core seen in panel 4IIa of Fig. 11 does tilt downward offshore, cutting across density surfaces with a tilt of about 10^{-2}. Its upper boundary weakens offshore with increased core depth. Another cold core spanning panels 6b,c in Fig. 13 shows the same tendencies, extending across isopycnals with a slope of $\approx 10^{-2}$ downward, northwest to southeast.

Strong horizontal gradients ($\sim 10^{-3}$ °C m^{-1}) sometimes mark the lateral core boundaries, as in panels 4Id of Fig. 11 and 7e of 13, which, judging from Turner's shadographs, is also consistent with the expected behavior of intrusions in a doubly diffusive system.

AN ANOMALOUS FEATURE

As pointed out earlier, when the warping of isopotential density surfaces is due primarily to causes other than internal waves, the techniques used here do not cleanly separate wave and glob variability. But a straightforward interpretation of the results nevertheless exists. What is labeled "wave effect", such as in the upper panel of Fig. 10, can in every case be interpreted as the displacement field of isopotential density surfaces about their mean depths. And what is labeled "glob effect", as in the second panel down in Fig. 10, always portrays the field of variability along isopotential density surfaces referenced to their rest depths.

There is a region in the data records where the displacements are not simple wave motion. It is unique in that it demonstrates a resolvable density instability. Panel 6b of Fig. 13 shows this peculiar feature. It is reproduced in Fig. 15 along with associated data. Centered at a range of 5.5 km in the second panel down in Fig. 15 is a column of cold fresh water. It is shaped somewhat like an hourglass whose boundaries are marked by sharp horizontal gradients. Symmetry about a vertical axis extends to either side for 2 km or more.

The density field in the lower panel of Fig. 15 shows, by the separation of isopycnals, that in the area of the cold column the density gradient is smaller than in the surrounding water. In fact, there is a density instability at the location of the narrowest part of the hourglass; the 26.985 σ_θ surface reappears 15 m or so below its first depth of encounter. Isopycnals above the instability are displaced upward, and those below it slightly downward. This can also be seen in the top panel of 15.

The corresponding temperature field shown in Fig. 15 indicates a plume of cold water extending upward from the depth of the density instability, with warmer water apparently displaced downward on either side of the plume.

The structure is suggestive of a large-scale convection with upward motion along the axis of symmetry.

7. Sound speed field

Readers not interested in the influence of oceanic variability on sound speed may skip sections 7 and 8 without loss.

We define a *potential* sound speed $\hat{C}$ such that

$$\hat{C}(x,z) = C(x,z) - \gamma\zeta(x), \qquad (28)$$

where γ is the adiabatic lapse rate for sound speed (~ 0.0164 s^{-1}). In the manner of Eq. (20) we may then write

$$\delta\hat{C}(x,z_0) = \hat{C}(x,z_{\rho_0}) - \hat{C}_0, \qquad (29)$$

where $\delta\hat{C}$ is the sound speed anomaly field one would see in the absence of waves.

The relative importance of salt and temperature to glob-induced sound speed irregularities is seen as

follows. From (18), we have $b\delta S = a\delta\theta$, and, furthermore, we may write

$$\delta\hat{C} = \delta\hat{\theta}(\partial C/\partial\theta) + \delta S(\partial C/\partial S). \qquad (30)$$

The ratio of saline to thermally induced sound speed fluctuations is then

$$c = \frac{\delta S(\partial C/\partial S)}{\delta\hat{\theta}(\partial C/\partial\theta)} = \frac{a\beta}{b\alpha}, \qquad (31)$$

where, for this case $\alpha = C^{-1}(\partial C/\partial\theta) = 2.5 \times 10^{-3}$ (°C)$^{-1}$, and $\beta = C^{-1}(\partial C/\partial S) = 7.7 \times 10^{-4}$ (‰)$^{-1}$, $C = 1510$ m s^{-1}, giving
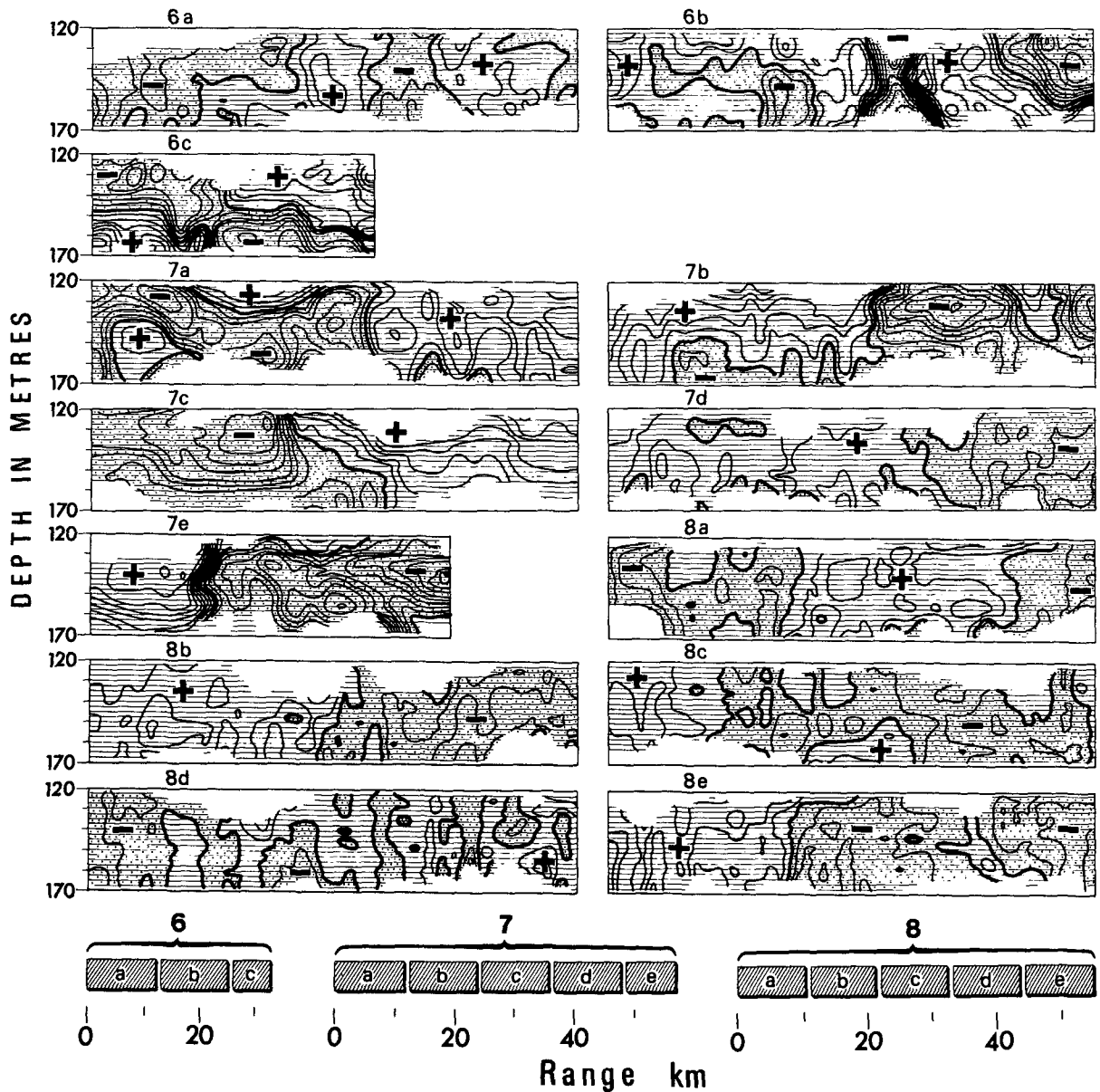

FIG. 13. Variations of the sea's properties due to inhomogeneities. Observations are along the alongshore tow paths. The lower bar graph shows the locations of the observations along the paths. Refer to Fig. 3 for path locations. The contours may be interpreted in terms of potential temperature ($\Delta\theta = 0.025°C$), salinity ($\Delta S = 6.3 \times 10^{-4}$ ‰) or potential sound speed ($\Delta\hat{C} = 0.1$ m s^{-1}). Viewing window excludes vertical wavelengths < 14 m and horizontal wavelengths < 250 m.

$$c = 0.08. \tag{32}$$

Figs. 10, 11 and 13 showing temperature (or salt) variability may be interpreted in terms of sound speed through Eqs. (30) and (31). That is,

$$\delta\hat{C} = \delta\hat{\theta}\alpha C(1 + c) \approx 4.0\delta\hat{\theta}. \tag{33}$$

By analogy with Eq. (26), the wave-caused disturbances in sound speed are estimated as

$$\delta\hat{C}_w(x,z_0) = (d\hat{C}/dz)\zeta(x), \tag{34}$$

in which the effects due to wave induced particle velocities and pressure changes are neglected, as shown feasible by Munk and Zachariasen (1976). Figs. 10, 12 and 14 showing the $\zeta(x,z)$ field may then be interpreted in terms of sound speed using the estimated gradient $d\hat{C}/dz = -0.04$ s^{-1} in Eq. (34). The contour interval for sound speed in Figs. 10–14 is therefore 0.1 m s^{-1}, and the magnitudes of variations in the figures may be intercompared directly.
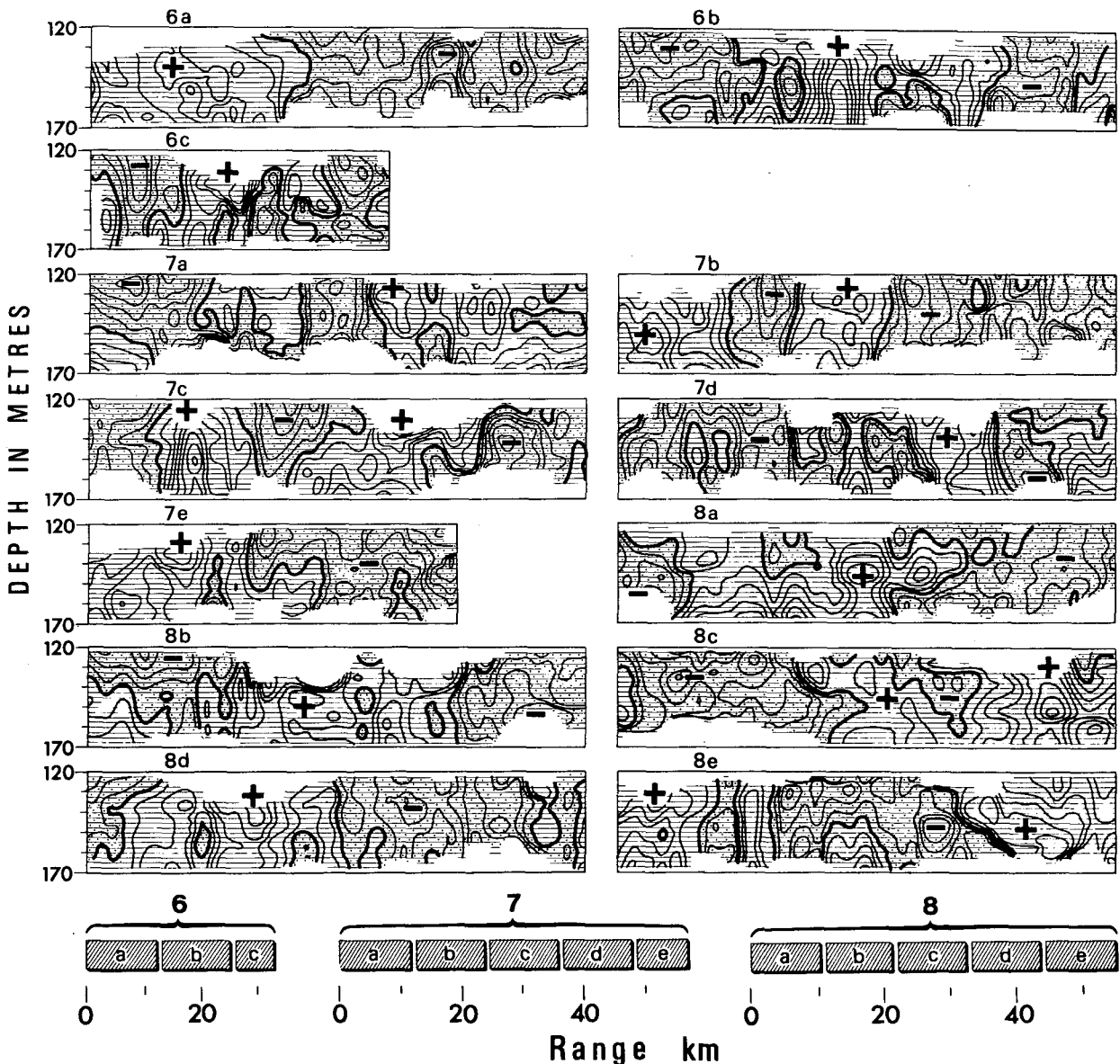
In analogy with our previous characterization

FIG. 14. The internal wave displacement field $\zeta(x,z)$. Observations are along the alongshore tow paths. The lower bar graphs show the locations of the observations along the paths. Refer to Fig. 3 for path locations. The contour interval $\Delta\zeta = 2.5$ m. These contours may also be interpreted in terms of the wave induced variability in the fields of salt ($\Delta S = -5.5 \times 10^{-3}$ ‰), potential temperature ($\Delta\hat{\theta} = -0.035$°C) or potential sound speed ($\Delta\hat{C} = -0.1$ m s^{-1}) by using relationships like Eq. (26). Viewing window excludes vertical wavelengths < 14 m and horizontal wavelengths < 250 m.
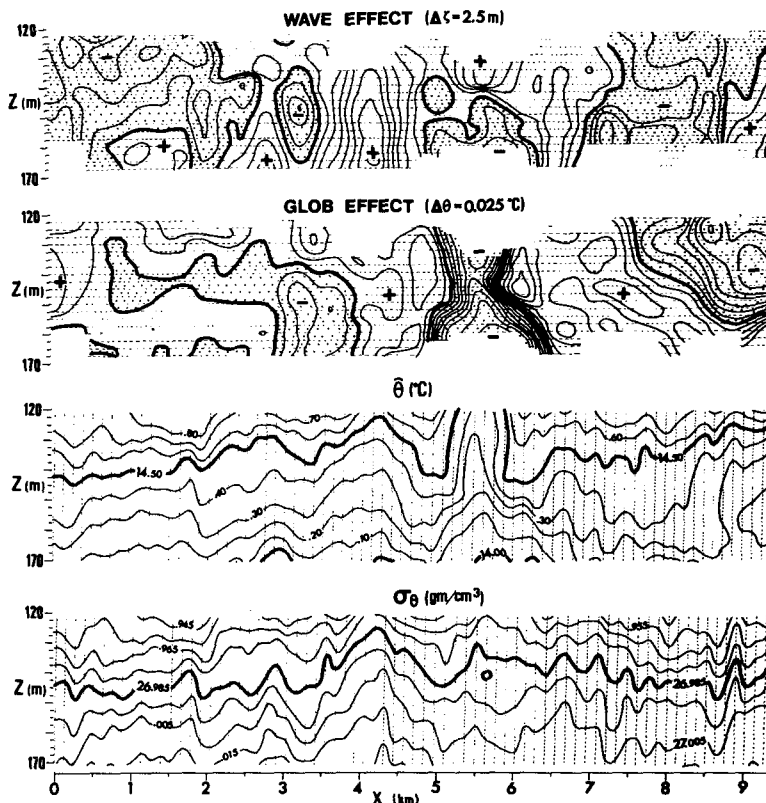
FIG. 15. Density and potential temperature fields from a part of tow segment 6.
Contour interval $\Delta\zeta$ = 2.5 m; $\Delta\hat{\theta}$ = 0.025°C.

of the irregularities in the Gulf, for sound speed we may say that the area is one in which there are rather large-scale cores of low sound speed water imbedded in a more uniform higher sound speed background. These cores are estimated to have lifetimes of weeks or more. Superimposed on this is a pattern of variability due to internal waves. Extremes of the two effects are about the same size, but the wave-induced fluctuations occur throughout the medium in patterns that may change from hour to hour.

8. Sound speed spectra

Spectral estimates of the fluctuations in sound speed along horizontal paths are made for the separate effects of globs and waves using definitions from Eqs. (29) and (34). Fig. 16 gives one example of the series $\delta\hat{C}(x,z_0)$, and $\delta\hat{C}_w(x,z_0)$ as well as the total variability measured along z_0 = 145 m. Multiplying by C_0^{-1} gives series of fractional sound speed fluctuations. The series exhibit nonstationarities of the mean, therefore their spectra were prewhitened and later adjusted to account for the very low wavenumber trends.

The resulting spectra are shown in Fig. 17. As already suggested by the curves in Fig. 16, the

spectral level of variability due to waves is nearly the same as the total. Globs contribute only about one-fifth as much variance as waves at wavenumbers > 10^{-4} cpm, and about one-half as much at
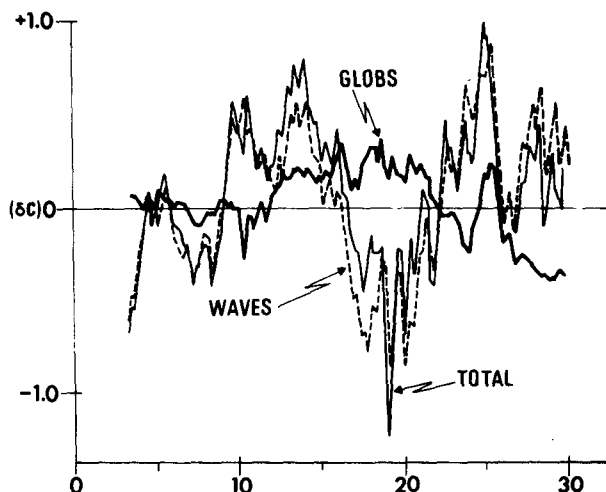

FIG. 16. An example of the total fluctuations in sound speed along z = 145 m compared to the fluctuations due solely to internal waves ($\delta\hat{C}_w$), and those due solely to globs ($\delta\hat{C}$). Data are from a portion of tow segment 3. Units for sound speed are m s^{-1}.
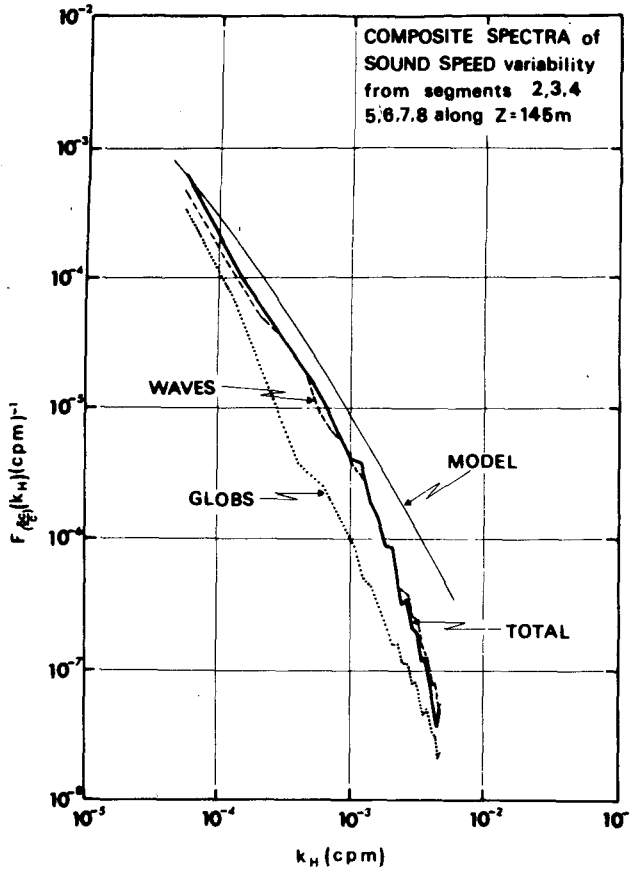
FIG. 17. Horizontal wavenumber spectrum of the total fractional sound speed fluctuations along $z = 145$ m, and the spectra of the fractional sound speed fluctuations due to waves $(\delta \hat{C}_w/C)$ and globs $(\delta \hat{C}/C)$ over the same paths. Degrees of freedom for each spectrum range from 12 to 96. Model estimated spectrum is from Munk and Zachariasen (1976).

lower wavenumbers. The glob spectrum goes very nearly as k_H^{-2} whereas the wave fluctuation spectrum goes rather more slowly at low wavenumbers and more quickly at high wavenumbers.

MODEL COMPARISON

The model estimate of the spectrum of sound speed fluctuations shown in Fig. 17 is from Munk and Zachariasen (1976). They find for the power spectrum of fractional sound speed fluctuations due to internal waves[3]

$$F_{(\delta \hat{C}_w/C)}(k_H, j)$$

$$= \left\langle \left(\frac{\delta \hat{C}_w}{C} \right)^2 \right\rangle \frac{2\pi^{-1}(\omega_i/N_0)B^{-1}k_H^2 jH(j)}{[(k_H)^2 + (\frac{1}{2}jB^{-1}\omega_i/N_0)^2]^2}, \quad (35)$$

---

[3] Our notation is slightly different from theirs. We use cyclical rather than circular wavenumbers for ease of comparison with the observed data. Here $C \equiv C_0$.

where j is mode number, and where

$$H(j) = (j^2 + j_*^2)^{-1}/ \sum_{j=1}^{\infty} (j^2 + j_*^2)^{-1}, \quad (36)$$

$$\sum_{j=1}^{\infty} H(j) = 1,$$

$$\sum_{j=1}^{\infty} (j^2 + j_*^2)^{-1} \approx \frac{1}{2}j_*^{-2}(\pi j_* - 1), \quad j_* \geq 1.$$

Then summing over all modes yields the wave-number spectrum

$$F_{(\delta \hat{C}_w/C)}(k_H) = \left\langle \left(\frac{\delta \hat{C}_w}{C} \right)^2 \right\rangle 2\pi^{-1}(\omega_i/N_0)B^{-1}$$

$$\times \sum_{j=1}^{\infty} \frac{k_H^2 jH(j)}{[(k_H)^2 + (\frac{1}{2}jB^{-1}\omega_i/N_0)^2]^2}, \quad (37)$$

where $B = 1000$ m, $j_* = 3$, and we use our local value of ω_i (=0.05 cph). From Munk and Zachariasen we make the estimates

$$\left. \begin{array}{l} N = N_0 e^{-z/B}, \quad (N_0 = 3 \text{ cph}) \\ \text{rms}(\delta \hat{C}_w/C) = \text{rms}(\delta \hat{C}_w/C)_0 (N/N_0)^{3/2} \end{array} \right\}, \quad (38)$$

where N is the buoyancy frequency and rms( ) is the root-mean-square value with

$$\left. \begin{array}{l} \text{rms}(\delta \hat{C}_w/C)_0 = (3.0 \times 10^{-6})\mu N_0^2 \text{rms}(\zeta_0)g^{-1} \\ \text{rms}(\zeta_0) = 7.3 \text{ m from Garrett and Munk} \\ (1972) \end{array} \right\}, \quad (39)$$

$$\mu = (\alpha/a)s(T_u). \quad (40)$$

In Eq. (12), $s = (1 + cT_u)$, where c is as defined previously [Eq. (31)], and where the Turner number is

$$T_u = \left(b \frac{\partial S}{\partial z} \right) / \left(a \frac{\partial \theta}{\partial z} \right).$$

Our gradients are typically $\partial S/\partial z = -2.2 \times 10^{-3}$ (‰) m^{-1} and $\partial \theta/\partial z = -1.4 \times 10^{-2}$ (°C) m^{-1}, yielding $T_u = 0.63$, and $s = 2.8$. From Eqs. (40), (39), (38), we calculate the model estimates $\mu = 22.0$, rms $(\delta \hat{C}_w/C)_0 = 4.5 \times 10^{-4}$, and rms $(\delta \hat{C}_w/C) = 3.6 \times 10^{-4}$. The estimated mean-squared value from the model is then

$$\left\langle \left(\frac{\delta \hat{C}_w}{C} \right)^2 \right\rangle = 1.3 \times 10^{-7}.$$

Replacing this in Eq. (37) gives us the Munk and Zachariasen model spectrum of internal-wave-induced fractional sound speed fluctuations shown in Fig. 17. It is to be compared to the spectrum of observed wave-induced fluctuations.

9. Discussion

The Gulf of Cadiz is a complex region influenced by the exchange of Atlantic and Mediterranean water. Abundant salinity and temperature observations have been taken over the years, in an attempt to better understand this exchange (cf. Zenk 1975a,b; Thorpe 1976). Pingree (1972) recognized that whereas spatial variations of salt and temperature occur rapidly and frequently in this zone, they do so primarily along surfaces of constant potential density, implying that intrusions play an important mixing role.

We have tried here to draw a clearer picture of this variability, sorting out the effects of internal waves and globs for separate examination.

The capability to profile while towing provides us with a unique two-dimensional (x,z) description of the fields of salt, temperature, density and sound speed.

The density field is adequately resolved over long tow paths to give internal wave horizontal wavenumber spectra in which the usual contamination of vertical and horizontal thermal structure is minimized. These "clean" spectra do not differ in any significant way from spectra in which the contamination due to horizontal structure has not been removed. While this is not a striking result, it is an important one, since it validates results based on simpler methods.

Identifying the effects of internal waves by their influence on the density field permits their removal from data records, and leaves a clear picture of the variability within the medium due simply to spatial differences in the physical makeup of the water. The picture of the area investigated is one in which there are large cores of cold fresh water scattered throughout a more uniform warmer saltier background. There is reason to believe that these cores have lifetimes of weeks or more.

The size and persistence of the cores, coupled with the fact that their boundaries are marked by relatively strong gradients, add interest to their presence in the sound speed field. While they do not contribute much to the *overall* sound speed variance, they may dominate it locally, in the form of well-defined ducts tens of meters thick and several kilometers wide.

As expected, the major source of sound speed variability is warping and straining of the medium due to internal waves. Comparison of the Munk and Zachariasen model spectrum of wave-induced sound speed fluctuations with the observations shows good agreement.

REFERENCES

Cairns, J. L., and G. O. Williams, 1976: Internal wave observations from a midwater float, 2. *J. Geophys. Res.*, **81**, 1943–1950.

Dashen, R., 1977: Path integrals for waves in random media. Tech. Rep. JSR-76-1, Stanford Research Institute, 112 pp.

Desaubies, Y. J. F., 1976: Analytical representation of internal wave spectra. *J. Phys. Oceanogr.*, **6**, 976–981.

Gargett, A. E., 1976: An investigation of the occurrence of oceanic turbulence with respect to finestructure. *J. Phys. Oceanogr.*, **6**, 139–156.

Garrett, C. J. R., and W. H. Munk, 1972: Space-time scales of internal waves. *Geophys. Fluid Mech.*, **2**, 225–264.

——, and W. H. Munk, 1975: Space-time scales of internal waves: A progress report. *J. Geophys. Res.*, **80**, 291–297.

Gregg, M. C., and C. S. Cox, 1972: The vertical microstructure of temperature and salinity. *Deep-Sea Res.*, **19**, 355–376.

——, C. S. Cox and P. W. Hacker, 1973: Vertical microstructure measurements in the central North Pacific. *J. Phys. Oceanogr.*, **3**, 458–469.

Howe, M. R., and R. I. Tait, 1970: Further observations of thermohaline stratification in the deep ocean. *Deep-Sea Res.*, **17**, 963–972.

——, and R. I. Tait, 1972: The role of the temperature inversions in the mixing processes of the deep ocean. *Deep-Sea Res.*, **19**, 781–791.

Johnson, C. L., C. S. Cox and B. Gallagher, 1978: The separation of wave induced and intrusion oceanic finestructure. *J. Phys. Oceanogr.*, **8**, 846–860.

Joyce, T. M., W. Zenk and J. M. Toole, 1978: The anatomy of the Antarctic polar front in the Drake Passage. *J. Geophys. Res.*, **83**, 6093–6113.

Munk, W. H., and F. Zachariasen, 1976: Sound propagation through a fluctuating stratified ocean: Theory and observations. *J. Acoust. Soc. Amer.*, **59**, 818–838.

Pingree, R. D., 1972: Mixing in the deep stratified ocean. *Deep-Sea Res.*, **19**, 549–561.

Stevenson, R. E., 1977: Huelva Front and Malaga, Spain Eddy chain as defined by satellite and oceanographic data. *Dtsch. Hydrogr. Z.*, **30**.

Thorpe, S. A., 1976: Variability of the Mediterranean undercurrent in the Gulf of Cadiz. *Deep-Sea Res.*, **23**, 711–727.

Turner, J. S., 1973: *Buoyancy Effects in Fluids.* Cambridge University Press, 367 pp.

Woods, J. D., and P. J. Minnett, 1979: Analysis of mesoscale thermoclinicity with an example from the tropical thermocline during GATE. *Deep-Sea Res.*, **26A**, 85–96.

Zenk, W., 1975a: On the Mediterranean outflow west of Gibraltar. *Meteor Forschungsergeb.*, **A16**, 23–24.

——, 1975b: On the origin of the intermediate double-maxima in T/S profiles from the North-Atlantic. *Meteor Forschungsergeb.*, **A16**, 35–43.